

## Simultaneous acquisition of functional magnetic resonance images and impedance cardiography

MATTHEW CIESLAK,<sup>a</sup> WILLIAM S. RYAN,<sup>a</sup> ALAN MACY,<sup>b</sup> ROBERT M. KELSEY,<sup>c</sup> JESSICA E. CORNICK,<sup>a</sup> MARLO VERKET,<sup>a</sup> JIM BLASCOVICH,<sup>a</sup> AND SCOTT GRAFTON<sup>a</sup>

<sup>a</sup>Department of Psychological and Brain Sciences, University of California, Santa Barbara, Santa Barbara, California, USA

<sup>b</sup>Biopac, Goleta, California, USA

<sup>c</sup>Memphis, Tennessee, USA

### Abstract

While simultaneous acquisition of electrocardiography (ECG) data during MRI is a widely used clinical technique, the effects of the MRI environment on impedance cardiography (ICG) data have not been characterized. We collected echo planar MRI scans while simultaneously recording ECG and thoracic impedance using carbon fiber electrodes and customized amplifiers. Here, we show that the key changes in impedance ( $dZ/dt$ ) and features of the ECG waveforms are not obstructed during MRI. We present a method for ensemble averaging ICG/ECG signals collected during MRI and show that it performs comparably with signals collected outside the MRI environment. These results indicate that ICG can be used during MRI to measure stroke volume, cardiac output, pre-ejection period, and left ventricular ejection time.

**Descriptors:** MRI, Impedance cardiography, Autonomic nervous system

There is a large and growing interest in the field of psychology, broadly defined, in measuring the physiological substrates of psychological states. Existing psychophysiological measures vary widely from those assessing central nervous system activation to those assessing the activation of peripheral physiological systems. Perhaps the most widely employed and most extensively validated method for noninvasively assessing central nervous system activation is fMRI, which has yielded important insights for understanding a diversity of social psychological processes including affect, emotion, attraction, social development, aggression, and altruism (Cacioppo, Berntson, Sheridan, & McClintock, 2000).

At the peripheral level, a wide variety of physiological processes can be indexed including those regulated by the parasympathetic and sympathetic branches of the autonomic nervous system (ANS), by neuroendocrine-mediated changes in hormone levels, by changes of immune responses, and by skeletal muscle activation (Blascovich & Mendes, 2010). Such processes can be assessed via measures of cardiovascular reactivity, including electrocardiographic (ECG) measures such as heart rate and heart rate variability (HRV), impedance cardiographic (ICG) measures such as cardiac output and

pre-ejection period (PEP), and blood pressure measures. These measures have been of particular interest as indices of cardiovascular health and efficiency when assessed at baseline or in relation to specific tasks (e.g., Kelsey, 2004; Lovallo & Gerin, 2003; Matthews, Salomon, Brady, & Allen, 2003). Additionally, these measures provide insight into motivational (Blascovich, 2013; Kelsey, 2012) and emotional (Kreibig, 2010) states.

Though these cardiovascular indices have been well validated (Mezzacappa, Kelsey, & Katkin, 1999; Seery, 2011; Tomaka, Blascovich, Kelsey, & Leitten, 1993), their relation to CNS activation has not. There has been much theorizing about the dynamic feedback relations between the central and peripheral nervous systems (e.g., Porges, 2007); however, little work has directly examined the structure and dynamics of this connection. Napadow and colleagues (2008) explored the neural correlates of central autonomic activity using a combined HRV and fMRI approach, and found that high frequency HRV was positively correlated with relative brain activation within multiple brain regions including the hypothalamus, amygdala, and dorsolateral prefrontal cortex, and negatively correlated with activity in the parabrachial nucleus and periaqueductal gray. Central control of the ANS has also been investigated using electrodermal activity, heart rate, and blood pressure to index autonomic activation (Butler et al., 2007; Critchley, 2009; Critchley, Melmed, Featherstone, Mathias, & Dolan, 2002; Gianaros & Sheu, 2009).

However, assessing central correlates of autonomic activation based on single-measure indices such as HRV has been shown to provide a limited basis for inference because peripheral measures (e.g., HR, HRV, skin conductance) are related to multiple physiological and psychological states (Cacioppo & Tassinary, 1990). Instead, multimeasure indices should be leveraged in order to home

This work was supported by the Institute for Collaborative Biotechnologies through contract no. W911NF-09-D-0001 from the U.S. Army Research Office. The authors would like to acknowledge the contributions of Mario Mendoza in establishing an optimal ECG electrode placement. We also appreciate the assistance of Viktoriya Babenko, Shelbi Thompson, Jessica Hai, Petra Rupert, and Suzanne Becker in collecting data. Kelsey Alcorn at the School of the Art Institute of Chicago created the artwork in Figure 2a.

Address correspondence to: Matthew Cieslak, Department of Psychological and Brain Sciences, University of California, Santa Barbara. Santa Barbara, CA 93106, USA. E-mail: matthew.cieslak@psych.ucsb.edu

in on specific psychophysiological processes and states. For example, by combining estimates of cardiac output and blood pressure, it is possible to assess vasomotor tone, which is mediated by sympathetic activity on a relatively fast time scale. Vasomotor tone is only one valuable measure of sympathetic activity that is provided by ECG/ICG, with PEP being the most obvious example.

The present work takes a major step toward enabling the study of dynamic interactions between the central and peripheral nervous systems by demonstrating the robust measurement of ICG and ECG signals within the MRI environment while scans are acquired. We detail the steps necessary to obtain these measures as well as the equipment and procedures required to collect these measures while minimizing risk to participants and interference between measurement techniques. Because others (Gianaros & Sheu, 2009; Okon-Singer et al., 2014) have already demonstrated the feasibility and validity of assessing continuous blood pressure during fMRI, we do not present blood pressure data here.

Impedance cardiographic data are typically used to calculate stroke volume and cardiac output based on the features of their ensemble-averaged waveforms (Kelsey & Guethlein, 1990; Kelsey et al., 1998; Sherwood, Dolan, & Light, 1990). To prove the interpretability of data collected during MRI, it must be shown that any MRI-related artifacts such as eddy currents do not fundamentally change the features used to calculate stroke volume (SV) and other ICG measures. To this end, we collected ECG/ICG on individuals at rest during MRI and outside of the magnetic field. Ensemble-averaged ICG measures were calculated over a variety of durations to mimic what could be used in a typical study of psychological states (Kelsey & Guethlein, 1990).

The effect of the ICG 4 mA current injection at 50 kHz on the MRI signal was not investigated. Although this small current is accompanied by a magnetic field, it is physically associated with the subject's torso, not the subject's head. The magnetic field strength drops off in proportion to  $\frac{1}{r^2}$ ; accordingly, this current should not materially affect imaging in the volume of the head. Furthermore, if there was a measurable impact, the fact that the current is steady state and at a precise frequency would permit removal with appropriate filtering from any obtained result.

## Method

### Participants

A total of 12 healthy, young adults (5 female, 7 male) participated in this 1-h study in exchange for US \$20 following the procedures described below. One female subject was dropped from analyses due to a particularly noisy signal that did not allow for accurate marking of inflection points. All participants provided informed consent, and the experimental protocol and procedures were approved by the institutional review board of University of California, Santa Barbara.

### Procedure

Upon arrival at the lab, participants completed a metal screening form in order to ensure that it was safe for them to enter the magnet. A research assistant then explained the purpose and general procedures of the study, and the participant signed a consent form detailing these procedures and all potential risks. A female research assistant applied the ECG and ICG electrodes. All ICG and ECG sensors were connected via carbon fiber wires to their respective hardware. Subjects were then positioned in the MRI scanner

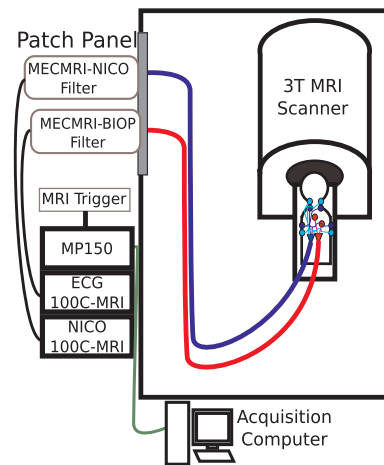


**Figure 1.** The layout of amplifiers and electrode leads. The MRI and its shielded environment are depicted inside a black rectangle. Subjects were fitted with 8 electrodes for ICG (cyan injected 4 mA at 50 kHz, blue recorded voltage). Carbon fiber electrodes and leads for ECG are depicted in red. ICG electrodes were connected via 15-cm carbon fiber leads to a 25-cm Y adapter into an 8-m insulated copper cable that connected to the patch panel. ECG electrodes were attached to an 8-m insulated copper cable connected to the patch panel. Both the ECG and ICG cables were met on the opposite side of the patch panel by hardware filters (MECMRI-BIOP for ECG and MECMRI-NICO for ICG). Finally, the filters were connected via 2-m cables to an MP150 amplifier system situated outside the MRI environment. The MP150 was connected to a computer in the MRI control room via an Ethernet cable.

(Figure 1 and completed a 15-min imaging protocol. Cardiovascular data were recorded during the 5-min echo planar imaging (EPI) sequence.

Following the scanning session, the participant was moved to a gurney outside the magnet room with all ECG and ICG electrodes and leads still attached. Five minutes of “control” cardiovascular data were then collected while the participant lay supine. After the recording was completed, all leads and electrodes were removed, and the participant was debriefed, paid, and thanked for participating. Participants were asked if they experienced any heat or skin irritation during the scans. No sensations of heat or electrode burns were reported.

### MRI Equipment and Imaging

A 3.0 T Siemens Trio with a 12-channel phased-array head coil was used for the acquisition of blood-oxygen-level-dependent (BOLD) signal. A single-shot EPI sequence that is sensitive to BOLD contrast was used to acquire 37 slices per repetition time (TR = 2000 ms, 3 mm thickness, 0.5 mm gap), echo time (TE) of 30 ms, flip angle of 90 degrees, field of view (FOV) of 192 mm, and 64 × 64 acquisition matrix. Prior to the acquisition of BOLD, a high-resolution T1-weighted sagittal sequence image of the whole brain was obtained (TR = 15.0 ms; TE = 4.2 ms; flip angle = 9 degrees, 3D acquisition, FOV = 256 mm; slice thickness = 0.89 mm, acquisition matrix = 256 × 256). The MRI signal quality was not compared with versus without the electrodes present, but no signal dropout or RF (radio frequency) artifact was observed in any image.

### Sensor Preparation and Placement

**ECG.** First, the areas where ECG electrodes were to be placed were cleaned and prepared with a small amount of Nu-Prep. Skin

preparation and electrode gel proved critical for obtaining robust measurements. Next, MRI-compatible, carbon fiber ECG electrodes were placed at the top of the sternum and at the bottom of the left pectoral muscle, consistent with the placement recommended for cardiac gated imaging (Figure 2a). We found this placement to produce a sharper QRS complex than the placement recommended

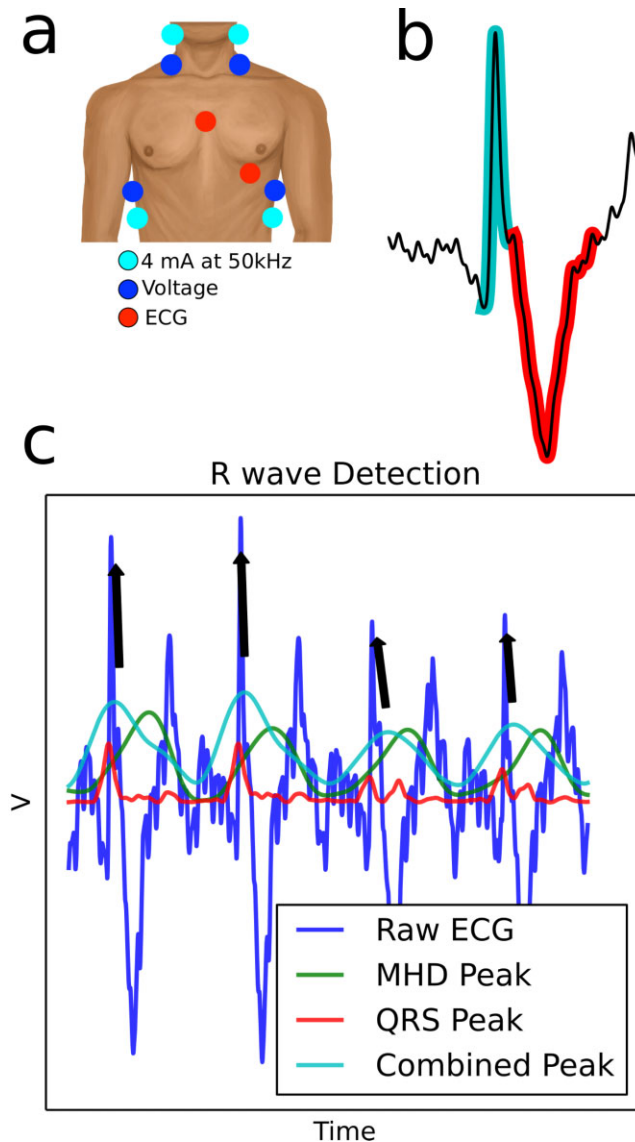


**Figure 2.** a: Electrode placement. Impedance cardiography used a set of four current-injecting electrodes (cyan) placed on the neck and torso and four voltage-sensing electrodes (blue) between the current injectors. ECG used a set of two electrodes (red) placed on the torso. b: The ECG signal in the magnetic field has two distinct components: the QRS complex (highlighted in light blue) and the magnetohydrodynamic (MHD) dip (highlighted in red). c: We altered the Pan-Tomkins algorithm to find peaks in the ECG frequency bands corresponding to both signal parts (red and green traces), then multiplied the resulting time series together (light blue) according to a weighting scheme. For subjects where the QRS amplitude was low, the QRS-weighted signal was downweighted relative to the MHD-related signal. The highest point in the raw ECG data immediately preceding the peak in the combined signal was labeled as the R wave (black arrows). Note that the T waves from the first two heartbeats are the same amplitude as the R waves from the last two, yet the algorithm finds all four heartbeats.

in Niendorf, Winter, and Frauenrath (2012). ECG signal quality was compared with the Siemens wireless ECG system for each subject to ensure that QRS complexes were detectable in the scanner bore. Since the wireless ECG does not work outside the scanner room, the scanning condition was always performed first.

**ICG.** In order to assess impedance cardiography, a total of eight carbon fiber electrodes were placed on the neck and torso of each participant: two on each side of the neck and two on each side of the torso (see Figure 2a). The upper neck and lower torso electrodes are current injecting, sending a 4 mA alternating current into the thoracic cavity at 50 kHz. The inner sets of electrodes are voltage sensing. The areas where the voltage electrodes were to be placed were prepared with Nu-Prep to increase signal integrity.

**Electrode composition.** Carbon fiber leads and electrodes were chosen for two major reasons: (1) to remove highly conductive materials from the vicinity of scanning, as large currents flowing in conductive materials may generate a local field, which may distort imaging; and (2) to establish high impedance leads to limit the flow of circulating currents during gradient switching and RF pulsing. The distributed resistance of the carbon fiber lead is optimal in comparison to a lumped impedance because the latter can exhibit parasitic capacitances that permit excessive RF current flow. The resistance of the carbon fiber leads is about 150 ohms/m, many thousands of times higher than the equivalent resistance exhibited by equivalently sized copper wire leads. This high resistance acts to reduce the quality factor of the circular conductive loop, consisting of the subject, electrodes, and leads, thereby reducing coupling to the incident RF energy. The high resistance of the carbon fiber leads also acts to restrict the flow of large circulating currents, as a consequence of magnetic field gradient shifts.

**Hardware and Amplifiers**

In order to minimize the noise introduced into the cardiovascular and hemodynamic signals by magnetic field gradient switching and RF pulses, specialized ECG and ICG amplifiers were built. The ECG amplifier (ECG100C-MRI, Biopac, Goleta, CA) had a slew rate limiter of approximately 300 mV/s, referenced to amplifier input. As specified by AAMI (Association for the Advancement of Medical Instrumentation), the maximum rate of change in the surface ECG is 280 mV/s. The ECG amplifier also incorporated additional filtering to reject signals associated with the 50 kHz excitation current sourced from the ICG amplifier. The ECG100C-MRI has 35 Hz low-pass-notch and 150 Hz low-pass filter options; these filters are second order Butterworth, 40 dB/decade. There are also high-pass filter options of 0.05 Hz and 1.0 Hz, and these filters are first order high-pass filters, 20 dB/decade.

The ICG amplifier (NICO100C-MRI, Biopac) was designed to measure conventional ICG parameters of thoracic impedance ( $Z$ ) and impedance change ( $dZ/dt$ ) with incorporated slew rate limiting of 5 ohms/s. The NICO100C-MRI has 10 Hz and 100 Hz low-pass filter options for  $Z$  and  $dZ$ , respectively; these filters are second order Butterworth, 40 dB/decade. There are also high-pass filter options for  $Z$  and  $dZ$ . These filter options are DC (no filter) and 0.05 Hz high-pass (first order, 20 dB/decade). The ICG amplifier employed a 50 kHz sinusoidal excitation current with magnitude of 4 mA rms.

Prior to amplification, all ECG and ICG leads were run through a common-mode, high frequency low-pass filter patch panel to suppress the influence of fMRI-generated RF interference on the

electrodes, leads, and cables. There are several linear, physically realized filters in the complete measurement setup. For bidirectional electromagnetic interference suppression, there are the previously discussed patch panel filters. These filters are two-stage low-pass filters that are associated with the MECMRI-NICO cable set. The filters are placed at the patch panel, and they have the following combined characteristics:

- Series inductance
- Shunt capacitance
- Cascaded Pi filters
  - $-3$  dB point = 400 kHz
  - Attenuation slope from 400 kHz to 7 MHz is 30 dB per decade
  - Attenuation is at least  $-60$  dB from 7 MHz to 1000 MHz

All signals were integrated using Biopac MP150 hardware and collected at 4 kHz sampling rate on a laptop computer running AcqKnowledge 4.3 (Biopac).

### Signal Processing

Magnetic field gradient switching generated electrical artifact at harmonics associated with scan frequencies (visible in Figure 3a, light gray lines). This artifact is a consequence of the magnetic field changing orientation in a conductive volume (the subject's torso). The NICO100C-MRI and ECG100C-MRI amplifiers detect this artifact. Both of these amplifiers are outfitted with nonlinear filters that are sensitive to the slope of the measured data. If the slope is higher than physiologically possible, the associated signal is limited to the highest slope allowed by the amplifier. RF sources, coincident with magnetic field gradient shifts, impact the measured

signal differently. In this case, the RF signal appears as a common-mode signal on the subject's body and the associated electrodes and leads. This common-mode RF signal travels to the MRI patch (filter) panel, where inline, common-mode filters establish a low impedance path to earth ground of the magnet (Figure 1). The filters at the patch panel are bidirectional, so that magnet-generated EMI (RF source) and control room EMI (from local computers and other equipment) are both trapped at the patch panel location. The  $dZ/dt$  signal was processed with a low-pass filter with a cutoff frequency of 15 Hz and a comb-stop filter at 18.5 Hz including all harmonics up to the Nyquist frequency. The ECG signal was not processed beyond the filters built into the amplifier.

We observed magnetohydrodynamic (MHD) effects on the ECG signal similar to those that have been previously reported (Abi-Abdallah, Robin, Drochon, & Fokapu, 2007; Fischer, Wickline, & Lorenz, 1999; Krug & Rose, 2011). The combination of MHD effects and EPI-related artifacts in the ECG signal made heartbeat detection difficult for traditional (Pan & Tompkins, 1985) methods that rely on the amplitude and frequency properties of the QRS complex. We developed a heartbeat detection algorithm that takes advantage of the reliability of the MHD effect when searching for heartbeats (Figure 2b). ECG signal was broken down into two derived signals, QRS power and MHD power. Both derived signals were created in the same way:

1. Band-pass filter the signal in the QRS (5–18 Hz) or MHD (0.05–0.5 Hz) frequency range.
2. Take the derivative of the signal squared.
3. Smooth the signal from step 2 with a Hanning window width of 100 ms (QRS) or 500 ms (MHD).

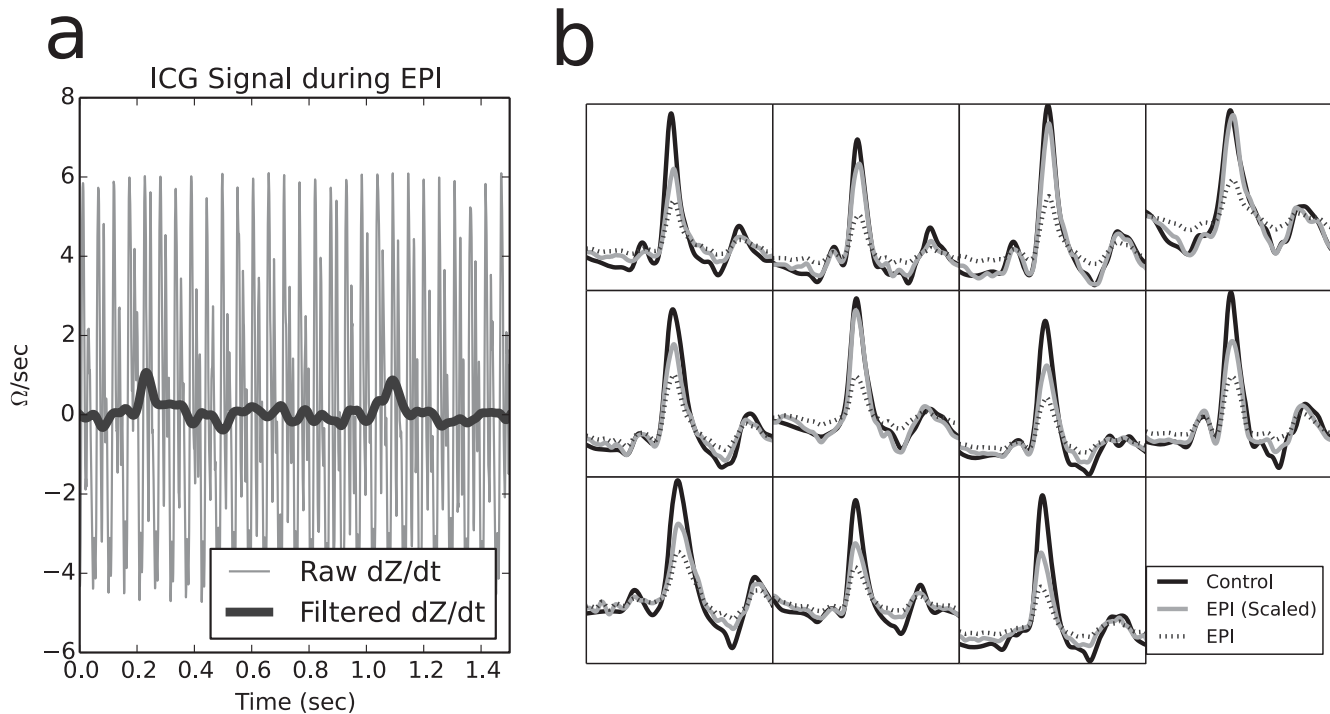


**Figure 3.** a: The  $dZ/dt$  signal accompanying two heartbeats that occurred during EPI is plotted. The raw signal in gray shows the characteristic sinusoidal artifact at 18.5 Hz. This same signal after filtering is plotted in black. b: Ensemble-averaged  $dZ/dt$  waveforms are plotted for all subjects. Ensemble averages from control data are plotted (black) against ensemble averages acquired during EPI (gray dashed). Ensemble averages acquired during EPI were scaled to account for the difference in base impedance to match the impedance value of each subject when outside the magnetic field (gray). The locations of critical features on each subject's ensemble-averaged waveforms are not different inside and outside the magnetic field. In some individuals, the  $Z_0$  amplitude correction did not fully account for the reduced impedance during scanning.

4. Multiply pointwise MHD power by QRS power, and smooth again with a 500-ms Hanning window. We found an optimal weighting scheme to be  $.8*QRS + 0.2*MHD$ .
5. Find peaks in step 4.
6. Manually create a peak amplitude threshold, and select only peaks above the threshold.
7. Inspect the 50 ms of raw ECG data preceding the peaks from step 6, and select the maximum point as the R wave.

After R peaks were detected in the ECG, signals were ensemble averaged over 300, 60, 30, and 15-s epochs. The ensemble-averaging technique (Kelsey & Guethlein, 1990) selects all R peaks within a time window and extracts the corresponding ECG,  $dZ/dt$ , and  $Z_0$  (base impedance) signals. Signals undergo time-locked averaging around the R peaks to produce an ensemble-averaged waveform. The ensemble-averaged waveform is inspected for characteristic points (e.g., the C, B, and X points on the  $dZ/dt$  average, and the P, Q, R, S, and T points on the ECG average). Time-locked averaging removes random noise and respiratory influences, and describes a characteristic heartbeat over the averaging epoch. The ensemble-averaged waveforms are used to calculate cardiovascular parameters such as left ventricular ejection time (LVET, time between the B and X points of  $dZ/dt$ ), PEP (time between the ECG R point and  $dZ/dt$  B point), and SV (see next section). We calculated PEP using the R to B interval rather than the more traditional Q to B interval because the magnetohydrodynamics of the MRI environment introduced noise to the ECG waveform that made detection of the Q point extremely difficult. Previous studies have established the reliability and validity of this abbreviated measure of PEP (Kelsey & Guethlein, 1990; Kelsey et al., 1998; Mezzacappa et al., 1999).

Ensemble averaging was performed using custom software written in Python. Waveform points were marked using an algorithm that first finds points on a “global ensemble average,” which is the ensemble average of all heartbeats contained in a recording. This global average is heavily attenuated due to signal variability, but provides a useful template for where that individual’s waveform features likely lie. The global ensemble average is used as a prior when marking points on individual ensemble-averaged wave-

forms (e.g., the ensemble averages of 15, 30, and 60 s). Point classifications made using this method were manually checked by a trained observer.

**Estimating Cardiovascular Parameters**

Ensemble-averaged waveforms were used to calculate cardiovascular measures such as heart rate (HR), LVET, PEP, SV, and cardiac output (CO, the product of  $HR \times [SV/1000]$ ). LVET and PEP are defined by components of both the ECG and ICG waveforms that do not depend on absolute signal amplitude.

Stroke volume is typically calculated from ensemble-averaged ICG waveforms using the Kubicek equation:

$$SV = \rho \frac{l^2}{Z_0^2} \times dZdt_{max} \times LVET$$

However, in our study, individuals’  $Z_0$  values were highly correlated during control and MRI measurements (linear regression,  $\beta = 0.57$ ,  $p < .001$ ; Pearson product moment,  $r = .82$ ,  $r^2 = .65$ ). This correlation, while high, is far from perfect. The  $\beta$  coefficient 0.57 indicates that the base impedance is nearly halved in the magnetic field. This is not a critical flaw in the ICG data acquired during MRI, since a linear difference can be mostly corrected. To correct for differences in basal impedance due to the MRI environment, a correction factor  $Z_c = \frac{\bar{Z}_{ctrl}}{\bar{Z}_{mri}}$  was applied to all terms that depend on  $Z_0$ , namely, the denominator and  $dZ/dt_{max}$ . The MRI-corrected stroke volume is then

$$SV_{MRI} = \rho \frac{l^2}{(Z_0 Z_c)^2} \times Z_c dZdt_{max} \times LVET,$$

which can be further simplified. All SV and CO values reported here were calculated using  $SV_{MRI}$ .

**Results**

Critically, the ensemble-averaged waveform features corresponded closely during MRI and control measurements (Figure 4). While

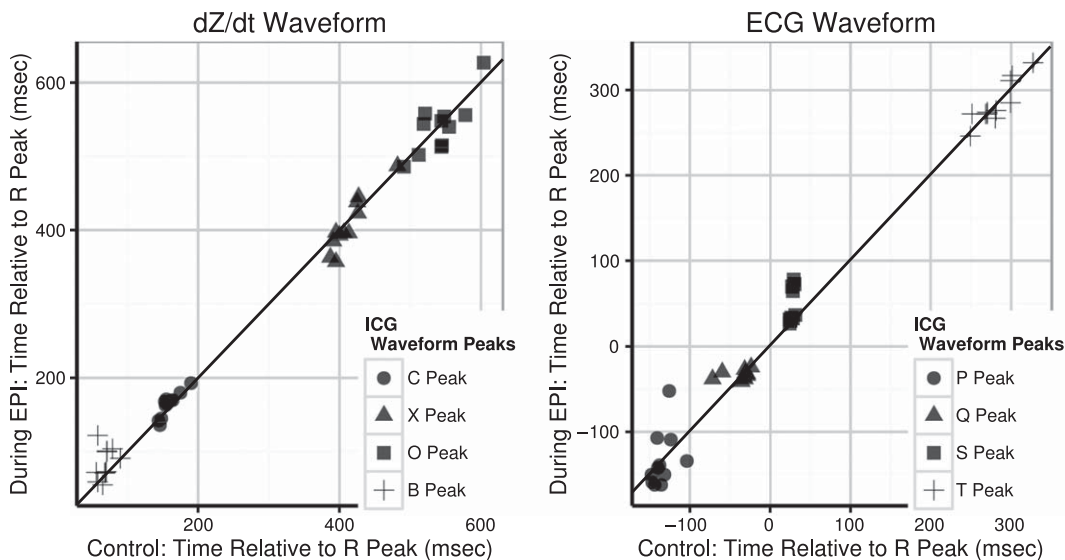


**Figure 4.** This figure shows the  $dZ/dt$  and ECG time points relative to the ECG R peak for each subject, based on 5-min ensemble averages.  $R = .997$ ,  $p < 10^{-16}$ .

**Table 1.** Cardiovascular Measures During Scanning and Control Conditions

Cardiovascular measure	60-s ensemble		30-s ensemble		15-s ensemble	
	(K = 55)		(K = 121)		(K = 231)	
	Control	Scanning	Control	Scanning	Control	Scanning
HR (bpm)						
Mean	61.10	58.86	59.56	56.39	60.92	58.34
SD	20.54	19.63	21.17	21.50	21.23	19.96
$SE_{meas}$		2.62		2.23		2.49
$r$		0.84**		.88***		.86***
ICC(2,K)		0.90***		.90***		.90***
PEP (ms)						
Mean	79.80	83.34	77.48	80.05	74.75	78.24
SD	21.15	22.11	19.41	20.36	19.56	20.56
$SE_{meas}$		3.82		2.55		2.42
$r$		0.80**		0.82**		0.85***
ICC(2,K)		0.88***		0.87**		0.87**
SV (ml)						
Mean	216.82	154.72	218.17	156.68	220.06	158.69
SD	43.98	43.39	46.10	43.77	46.96	44.41
$SE_{meas}$		20.21		19.90		18.20
$r$		0.84**		0.84**		0.87***
ICC(2,K)		0.64 <sup>†</sup>		0.65*		0.67*
CO (l/min)						
Mean	13.26	9.14	13.07	8.87	13.42	9.28
SD	15.79	15.41	15.66	15.59	15.58	15.44
$SE_{meas}$		1.53		1.42		1.37
$r$		0.80**		0.82**		0.83**
ICC(2,K)		0.62 <sup>†</sup>		0.62 <sup>†</sup>		0.64 <sup>†</sup>
LVET (ms)						
Mean	333.48	328.07	335.93	331.00	338.67	331.04
SD	28.08	33.19	29.65	37.60	28.80	37.09
$SE_{meas}$		5.72		3.69		4.14
$r$		0.89***		0.96***		0.94***
ICC(2,K)		0.91***		0.95**		0.93**
Z <sub>0</sub> Max						
Mean	21.17	21.17	21.16	21.15	21.17	21.16
SD	21.04	21.07	20.93	20.96	20.90	20.92
$SE_{meas}$		0.03		0.04		0.03
$r$		0.99***		0.99***		0.99***
ICC(2,K)		0.99***		0.99***		0.99***
dZ/dt Max						
Mean	1.59	1.12	1.58	1.12	1.59	1.14
SD	18.74	18.68	18.64	18.59	18.61	18.55
$SE_{meas}$		0.18		0.17		0.17
$r$		0.82**		0.83**		0.82**
ICC(2,K)		0.63 <sup>†</sup>		0.65 <sup>†</sup>		0.66*

Note. Values for PEP were calculated using R-B intervals.

\*\*\* $p < .001$ . \*\* $p < .01$ . \* $p < .05$ . <sup>†</sup> $p < .10$ .

the data presented in Figure 4 were derived from 5-min ensemble averages, the point relations were comparable for ensemble averages over 60-s ( $r = .998$ ,  $p < .0001$ ), 30-s ( $r = .997$ ,  $p < .0001$ ), and 15-s ( $r = .983$ ,  $p < .0001$ ) epochs.

Intraclass correlation coefficients (ICCs) for measurement agreement with subject as a random effect and Pearson correlation coefficients were calculated for LVET, PEP, SV, and CO. The ICCs and correlations between scanning and control recordings were significant for all measures (Table 1).

### Discussion

The results indicated a strong correlation between base impedance values during scanning and control sessions, but values during scanning were about half of those during control. Moreover, the shape of the dZ/dt waveform did not fundamentally differ between

these two conditions, and the timings of the critical points were strongly correlated. Estimates of cardiovascular parameters were generally consistent within individuals. Taken together, these results indicate the reliability and validity of assessing ICG during fMRI. Critically, the differences between measurements inside and outside the scanner can be at least partially corrected with simple rescaling. However, there remain unexplained differences in amplitude that could be due to ensemble averaging a noisier signal inside the scanner. The notably lower ICCs compared to Pearson's correlations ( $r$ ) for SV, CO, and dZ/dt max suggest that absolute amplitude values were discrepant between MRI and control measurements despite the linear adjustment based on Z<sub>0</sub>. Pearson's  $r$  is a measure of relative rank and thus does not take into account the discrepancies in absolute values between pairs. In contrast, the random effects ICC takes into account both the rank order and the absolute agreement for pairs. A comparison of  $r$ s and ICCs

indicates more discrepancy for the amplitude-based ICG measures than for the time-based measures, as expected. Thus, the scaling factor does not appear to work equally well when applied to  $dZ/dt$ . Moreover, further replication would be necessary to determine whether the specific beta weight adjustment applied here generalizes to other samples and measurement systems. It may still be that measurements of relative change in cardiovascular measures of interest (task – baseline deltas) will correspond well between MRI and control contexts, but that was not tested here, and thus requires further evaluation.

Psychological differences due to being inside versus outside the magnet were not examined in the present study, and thus appear in our data as noise. Future studies should investigate whether the experience of stress during MRI procedures influences physiological responses, creating differences between these conditions within some individuals. The investigation of this question is critical because, if there is indeed significant cardiovascular reactivity due to stress in the scanner for some participants, then this activation would need to be disentangled from activation due to the task at hand.

The EPI sequence, repetition time (2 s), and number of slices used in this study is one of the most widely adopted in fMRI research. The sinusoidal artifact created by our EPI was outside the frequency band of interest for ICG signal and therefore easy to filter out. Thus, the approach should be applicable to many fMRI laboratories. That said, there will likely be EPI sequences where the current filtering approach will not be effective. Reducing the number of slices per TR is one potential problem. Initial testing with a 22-slice (rather than 37-slice) 2,000 ms TR EPI sequence moved the EPI sinusoidal artifact into the frequency range of meaningful ICG—making artifact removal problematic. As long as the EPI gradient switching occurs at 18 Hz or higher, it should be easily removable with a similar recording system. This concern will likely diminish as fMRI centers adopt faster acquisition methods, such as multiband imaging. Our filtering method may

not generalize to other fMRI EPI sequences such as spiral imaging or multishot/multiecho imaging. In terms of risk, there was no evidence of heating at 3 Tesla with the impedance leads. However, it is possible that heating will be evident at 7 Tesla. It may be advisable to construct a body phantom test to evaluate circulating currents at high field strengths prior to human subject experiments.

The demonstrated ability to collect ICG and fMRI simultaneously has important implications for studying the dynamic relations between the peripheral and central nervous systems. This approach allows for elucidation of the direct afferent and efferent connections between cortical areas and the autonomic nervous system, including and in addition to well-established hypothalamic circuits.

The integration of these methods also has implications for the study of motivation and emotion. Though cognitive neuroscience studies employing fMRI have not controlled continuously and synchronously for approach-avoidance type motivational states, it is likely that such states influence cognitive processes. Integrating cardiovascular measures with fMRI provides a method for monitoring, studying, and covarying such influences on BOLD signal data, thereby isolating activation of BOLD signals due to other processes of interest. Furthermore, although many researchers employ peripheral physiological measures in studies of emotion (Kolodyazhniy, Kreibig, Gross, Roth, & Wilhelm, 2011; Kreibig, Wilhelm, Roth, & Gross, 2007; Stephens, Christie, & Friedman, 2010), the validity of such measures for indexing specific emotions has not been well established. Relating brain regions known to be involved in specific emotions to peripheral physiological activity could assist researchers in identifying reliable and valid peripheral indexes. Although additional research is needed to address the  $dZ/dt$  scaling discrepancy, the present research suggests that impedance cardiography during MRI can be a valid and powerful technique for measuring central and autonomic nervous system activity.

## References

- Abi-Abdallah, D., Robin, V., Drochon, A., & Fokapu, O. (2007). Alterations in human ECG due to the magnetohydrodynamic effect: A method for accurate R peak detection in the presence of high MHD artifacts. *Proceedings of the Annual International Conference of the IEEE Engineering in Medicine and Biology*, 1842–1845.
- Blascovich, J. (2013). Challenge and threat. In A. J. Elliot (Ed.), *Handbook of approach and avoidance motivation*, (pp. 431–445). New York, NY: Psychology Press.
- Blascovich, J., & Mendes, W. B. (2010). Social psychophysiology and embodiment. In S. T. Fiske, D. T. Gilbert, & G. Lindzey (Eds.), *The handbook of social psychology* (5th ed., pp. 194–227). New York, NY: Wiley.
- Butler, T., Pan, H., Tuescher, O., Engelen, A., Goldstein, M., Epstein, J., . . . Silbersweig, D. A. (2007). Human fear-related motor neurocircuitry. *Neuroscience*, 150, 1–7. doi: 10.1016/j.neuroscience.2007.09.048
- Cacioppo, J. T., Berntson, G. G., Sheridan, J. F., & McClintock, M. K. (2000). Multilevel integrative analyses of human behavior: Social neuroscience and the complementing nature of social and biological approaches. *Psychological Bulletin*, 126, 829–843.
- Cacioppo, J. T., & Tassinary, L. G. (1990). Inferring psychological significance from physiological signals. *American Psychologist*, 45, 16–28.
- Critchley, H. D. (2009). Psychophysiology of neural, cognitive and affective integration: fMRI and autonomic indicants. *International Journal of Psychophysiology*, 73, 88–94.
- Critchley, H. D., Melmed, R. N., Featherstone, E., Mathias, C. J., & Dolan, R. J. (2002). Volitional control of autonomic arousal: A functional magnetic resonance study. *NeuroImage*, 16, 909–919.
- Fischer, S. E., Wickline, S. A., & Lorenz, C. H. (1999). Novel real-time R-wave detection algorithm based on the vectorcardiogram for accurate gated magnetic resonance acquisitions. *Magnetic Resonance in Medicine*, 42, 361–370.
- Gianaros, P. J., & Sheu, L. K. (2009). A review of neuroimaging studies of stressor-evoked blood pressure reactivity: Emerging evidence for a brain-body pathway to coronary heart disease risk. *NeuroImage*, 47, 922–936.
- Kelsey, R. M. (2004). Heart disease and reactivity. In N. B. Anderson (Ed.), *Encyclopedia of Health and Behavior* (pp. 510–517). Thousand Oaks, CA: Sage Publications.
- Kelsey, R. M. (2012). Beta-adrenergic cardiovascular reactivity and adaptation to stress: The cardiac prejection period as an index of effort. In R. A. Wright & G. H. E. Gendolla (Eds.), *How motivation affects cardiovascular response: Mechanisms and applications* (pp. 43–60). Washington, DC: American Psychological Association.
- Kelsey, R. M., & Guethlein, W. (1990). An evaluation of the ensemble averaged impedance cardiogram. *Psychophysiology*, 27, 24–33.
- Kelsey, R. M., Reiff, S., Wiens, S., Schneider, T. R., Mezzacappa, E. S., & Guethlein, W. (1998). The ensemble-averaged impedance cardiogram: An evaluation of scoring methods and interrater reliability. *Psychophysiology*, 35, 337–340.
- Kolodyazhniy, V., Kreibig, S. D., Gross, J. J., Roth, W. T., & Wilhelm, F. H. (2011). An affective computing approach to physiological emotion specificity: Toward subject-independent and stimulus-independent classification of film-induced emotions. *Psychophysiology*, 48, 908–922.
- Kreibig, S. D. (2010). Autonomic nervous system activity in emotion: A review. *Biological Psychology*, 84, 394–421.

- Kreibig, S. D., Wilhelm, F. H., Roth, W. T., & Gross, J. J. (2007). Cardiovascular, electrodermal, and respiratory response patterns to fear- and sadness-inducing films. *Psychophysiology*, *44*, 787–806.
- Krug, J. W., & Rose, G. (2011). Magneto-hydrodynamic distortions of the ECG in different MR scanner configurations (pp. 769–772). *Proceedings of the Computing in Cardiology, 2011, conference*, Hangzhou, China.
- Lovallo, W. R., & Gerin, W. (2003). Psychophysiological reactivity: Mechanisms and pathways to cardiovascular disease. *Psychosomatic Medicine*, *65*, 36–45.
- Matthews, K. A., Salomon, K., Brady, S. S., & Allen, M. T. (2003). Cardiovascular reactivity to stress predicts future blood pressure in adolescence. *Psychosomatic Medicine*, *65*, 410–415.
- Mezzacappa, E. S., Kelsey, R. M., & Katkin, E. S. (1999). The effects of epinephrine administration on impedance cardiographic measures of cardiovascular function. *International Journal of Psychophysiology*, *31*, 189–196.
- Napadow, V., Dhond, R., Conti, G., Makris, N., Brown, E. N., & Barbieri, R. (2008). Brain correlates of autonomic modulation: Combining heart rate variability with fMRI. *NeuroImage*, *42*, 169–177.
- Niendorf, T., Winter, L., & Frauenrath, T. (2012). Electrocardiogram in an MRI environment: Clinical needs, practical considerations, safety implications, technical solutions and future directions (pp. 309–324). In R. M. Millis (Ed.), *Advances in electrocardiograms—Methods and analysis, InTech*, 2012.
- Okon-Singer, H., Mehnert, J., Hoyer, J., Hellrung, L., Schaare, H. L., Dukart, J., & Villringer, A. (2014). Neural control of vascular reactions: Impact of emotion and attention. *Journal of Neuroscience*, *34*, 4251–4259.
- Pan, J., & Tompkins, W. J. (1985). A real-time QRS detection algorithm. *IEEE Transactions on Bio-Medical Engineering*, *32*, 230–236.
- Porges, S. W. (2007). The polyvagal perspective. *Biological Psychology*, *74*, 116–143.
- Seery, M. D. (2011). Challenge or threat? Cardiovascular indexes of resilience and vulnerability to potential stress in humans. *Neuroscience and Biobehavioral Reviews*, *35*, 1603–1610.
- Sherwood, A., Dolan, C. A., & Light, K. C. (1990). Hemodynamics of blood pressure responses during active and passive coping. *Psychophysiology*, *27*, 656–668.
- Stephens, C. L., Christie, I. C., & Friedman, B. H. (2010). Autonomic specificity of basic emotions: Evidence from pattern classification and cluster analysis. *Biological Psychology*, *84*, 463–473.
- Tomaka, J., Blascovich, J., Kelsey, R. M., & Leitten, C. L. (1993). Subjective, physiological, and behavioral effects of threat and challenge appraisal. *Journal of Personality and Social Psychology*, *28*, 248–260.

(RECEIVED September 12, 2014; ACCEPTED October 25, 2014)